UPPSALA
UNIVERSITET

Simulation of Klein-tunneling in Graphene

Daniel Salvador, Fredrik Härlin

Project in Computational Science - Report #14

January 2015

PROJECT REPORT

Department of Information Technology

Abstract

We study the dynamics of Klein-tunneling in single-layer graphene. In particular we compare the numerical transmission probabilities of time-dependent wave-packets across a potential barrier with the analytical plane wave time-independent results presented in [3].

A strictly stable high-order accurate finite difference scheme for the simulation of time-dependent Klein-tunneling in single-layer graphene is constructed using the Summation-by-Parts–Simultaneous Approximation Term (SBP–SAT) method.

Particle transmission probabilities are obtained for angles of incidence between 0° and 75°. It is observed that the numerical transmission coefficient decays with an increasing angle of incidence, which does not agree with the analytical stationary results. Experiments with different wave-packet sizes indicate that localization is not responsible for the discrepancy; thus it must be caused by time-dependence. This suggests that time-dependent models are essential even for a qualitative understanding of Klein-tunneling in graphene.

Keywords: Klein-tunneling · Single-layer graphene · Massless Dirac fermions · High-order finite difference methods · SBP-SAT.

Contents

1 Introduction

The tunnel effect of a particle traveling through a potential barrier is a well-known phenomenon in quantum mechanics. When modeled with the non-relativistic Schrödinger equation, the probability that a particle crosses the barrier decays exponentially with the increase of the width and height of the barrier. However, if relativistic effects are taken into account, and instead one uses the massive Dirac equation to model this phenomenon, then the particle travels through the potential barrier with a certain probability which does not tend to zero regardless of the width and the potential height of the barrier [1]. This effect is called Klein-tunneling, after being theoretically described by Oskar Klein, a Swedish physicist, in 1929. See the illustration in Figure 1 for a conceptual description of a possible setting for Klein-tunneling.

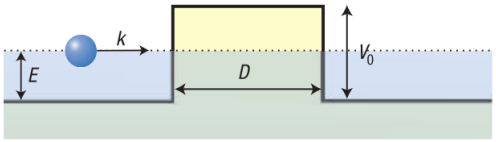

Figure 1: Illustration of a particle with energy E and momentum k traveling towards a potential barrier greater than its own energy, figure from [3].

Recent research has predicted this phenomenon for massless Dirac fermions in single-layer graphene. The 2-D honeycomb lattice structure of single-layer graphene is a possible physical environment for testing Klein-tunneling experimentally and the behavior of this type of fermions in this context can be modeled by the equation

$$i\hbar\psi_t = -i\hbar\nu_F\hat{\boldsymbol{\sigma}} \cdot \nabla\psi + V_0\psi, \tag{1.1}$$

which is further described in the next section.

The aim of this work is to study the dynamics of Klein-tunneling in single-layer graphene by solving a time-dependent problem with an efficient numerical method and then to compare the results with the theoretical plane wave time-independent results presented in [3]. Our report describes one method to numerically simulate dynamical fermions as wave-packets, by solving (1.1). An analysis of the transmission probability of fermions across a potential barrier as a function of angle of incidence is also presented.

The numerical simulations are performed using a Summation-by-Parts–Simultaneous Approximation Term (SBP–SAT) finite difference scheme as the discretization method for the spatial domain and a fourth order Runge-Kutta method for time-integration. There are several reasons to use SBP–SAT. Firstly, the summation-by-parts property of SBP operators, combined with the SAT boundary treatment, leads to discrete energy estimates that mimic the continuous energy estimates, and strict stability of the scheme can be proven. Moreover, the existence of high-order accuracy SBP operators provides a practical way of attaining a global high-order convergence rate. This proves to be crucial since high-order of accuracy schemes yield low dispersion errors, which makes them adequate for propagating disturbances over long distances. Additionally, by using SBP–SAT, important properties of a single-block configuration, such as

strict stability and accuracy, are preserved upon extension to multi-block geometries. The method has also been used previously to successfully simulate similar effects for massive Dirac fermions, see for example [2].

This report contains five sections. In the second section, the Equation (1.1) describing massless Dirac fermions in single-layer graphene is contextualized and analytical solutions for the plane wave case are derived. The third section contains the complete problem set-up in a 1-D domain, with an analysis of both well-posedness and error convergence rates for SBP operators of several orders of accuracy. In addition, numerical simulations of Klein-tunneling are performed and the results are compared to those obtained in [3]. The fourth section expands the definitions and analysis in the third section to two dimensions. In the fifth and final section, some conclusions regarding the results are drawn.

2 The equation

Due to graphene's particular material properties, charge carriers near the Fermi energy behave like 2-D massless relativistic particles (Dirac fermions), its energy being described by the linear dispersion relation

$$E = \hbar||\boldsymbol{k}||\nu_F, \tag{2.1}$$

where $\boldsymbol{k}$ is the wavevector and $\nu_F \approx 10^6\, ms^{-1}$ is the Fermi velocity. As a consequence, at low energies, the electrons in single-layer graphene can be described by the Dirac-like equation

$$i\hbar\boldsymbol{\psi}_t = -i\hbar\nu_F\hat{\boldsymbol{\sigma}}\cdot\nabla\boldsymbol{\psi} + V_0\boldsymbol{\psi}, \tag{2.2}$$

where $\hat{\boldsymbol{\sigma}} = (\sigma_x, \sigma_y)$ is the 2-D vector of Pauli matrices

$$\sigma_x = \begin{bmatrix} 0 & 1 \\ 1 & 0 \end{bmatrix},\ \sigma_y = \begin{bmatrix} 0 & -i \\ i & 0 \end{bmatrix},$$

and V_0 is the height of the potential barrier.

Considering a rectangular subdomain of $\mathbb{R}^2$,

$$\Omega_{w,s}^{e,n} = \left\{(x,y) \in \mathbb{R}^2 : w \le x \le e\,; s \le y \le n\right\},$$

the equation (2.2) describing massless Dirac fermions takes the form

$$\boldsymbol{\psi}_t + A\boldsymbol{\psi}_x + B\boldsymbol{\psi}_y = -(i/\hbar)V_0\boldsymbol{\psi}, \quad t \ge 0, \quad (x,y) \in \Omega_{w,s}^{e,n}, \tag{2.3}$$

where

$$A = \begin{bmatrix} 0 & \nu_F \\ \nu_F & 0 \end{bmatrix},\ B = \begin{bmatrix} 0 & -i\nu_F \\ i\nu_F & 0 \end{bmatrix}.$$

2.1 Analytical Solution

For the case of a particle free in space, that is, in the absence of a potential, when $V_0 = 0$, solutions to (2.3) can be found if we consider $\boldsymbol{\psi}$ to be a 2-D plane wave, whose general form is

$$\boldsymbol{\psi}(\boldsymbol{r}, t) = \boldsymbol{\psi}_0 e^{i(\boldsymbol{k}\cdot\boldsymbol{r} - \omega t)}, \tag{2.4}$$

where $\boldsymbol{r} = (x, y)$, $\boldsymbol{\psi}_0 = \left(\psi_0^{(1)}, \psi_0^{(2)}\right)$, $\boldsymbol{k} = \left(k^{(1)}, k^{(2)}\right)$ denotes the wave vector and ω is the angular frequency. Moreover, for a plane wave with Fermi velocity ν_F, these two latter physical quantities are related by the dispersion relation

$$\omega^2 = \nu_F^2 \left({k^{(1)}}^2 + {k^{(2)}}^2 \right). \tag{2.5}$$

Plugging the general 2-D plane wave expression (2.4) into Eq. (2.3) and solving for $\boldsymbol{\psi}$, we arrive at a linear system which, bearing in mind the dispersion relation (2.5), yields two possible solutions

case I: $\omega = -\nu_F \sqrt{{k^{(1)}}^2 + {k^{(2)}}^2}$

$$\Rightarrow \boldsymbol{\psi}(\boldsymbol{r}, t) = \begin{bmatrix} 1 \\ -\frac{k^{(1)} + ik^{(2)}}{\sqrt{{k^{(1)}}^2 + {k^{(2)}}^2}} \end{bmatrix} e^{i\left(\boldsymbol{k}\cdot\boldsymbol{r} + \nu_F \sqrt{{k^{(1)}}^2 + {k^{(2)}}^2} t\right)}; \tag{2.6}$$

case II: $\omega = +\nu_F \sqrt{{k^{(1)}}^2 + {k^{(2)}}^2}$

$$\Rightarrow \boldsymbol{\psi}(\boldsymbol{r}, t) = \begin{bmatrix} 1 \\ \frac{k^{(1)} + ik^{(2)}}{\sqrt{{k^{(1)}}^2 + {k^{(2)}}^2}} \end{bmatrix} e^{i\left(\boldsymbol{k}\cdot\boldsymbol{r} - \nu_F \sqrt{{k^{(1)}}^2 + {k^{(2)}}^2} t\right)}. \tag{2.7}$$

2.2 Steger-Warming Flux Splitting

The matrices A and B in the system (2.3) are Hermitian , i.e. $A = A^*$ and $B = B^*$. Thus, they can be diagonalized by the unitary similarity transformations T_A and T_B, respectively, that is, we can write

$$A = T_A \Lambda_A T_A^*, \quad B = T_B \Lambda_B T_B^*,$$

where $\Lambda_A = diag(-\nu_F, +\nu_F) = \Lambda_B$, since $\sigma(A) = \{\pm\nu_F\} = \sigma(B)$, and

$$T_A = \frac{1}{\sqrt{2}} \begin{bmatrix} -1 & 1 \\ 1 & 1 \end{bmatrix}, \quad T_B = \frac{1}{\sqrt{2}} \begin{bmatrix} -i & 1 \\ i & 1 \end{bmatrix}.$$

We can use the *Steger-Warming* flux splitting to split A and B into positive and negative parts, $A = A_+ + A_-$ and $B = B_+ + B_-$ by defining

$$A_\pm = T_A^* \left(\frac{\Lambda_A \pm |\Lambda_A|}{2} \right) T_A, \quad B_\pm = T_B^* \left(\frac{\Lambda_B \pm |\Lambda_B|}{2} \right) T_B.$$

Note that A_+ and B_+ are Hermitian positive semidefinite (HPSD), while A_- and B_- are Hermitian negative semidefinite (HNSD). This splitting will prove to be very useful to conveniently define appropriate boundary conditions for our problem.

3 The 1-D Problem

In one dimension, the equation describing massless Dirac fermions in single layer graphene can be written

$$\boldsymbol{\psi}_t + A\boldsymbol{\psi}_x = -(i/\hbar) V_0 \boldsymbol{\psi}. \tag{3.1}$$

Considering the domain $\Omega = [0,1]$ and bearing in mind the Steger-Warming flux splitting defined in Section 2.2, we can impose boundary conditions on the ingoing characteristic variables by specifying $A_+\boldsymbol{\psi}$ and $A_-\boldsymbol{\psi}$ at the left and right boundaries, respectively. We then obtain the 1-D problem

$$\begin{cases} \boldsymbol{\psi}_t + A\boldsymbol{\psi}_x = -(i/\hbar)V_0\boldsymbol{\psi}, & x \in \Omega, \quad t > 0, \\ A_+\boldsymbol{\psi} = A_+\boldsymbol{g}_0(t), & x = 0, \quad t \geq 0, \\ A_-\boldsymbol{\psi} = A_-\boldsymbol{g}_N(t), & x = 1, \quad t \geq 0, \\ \boldsymbol{\psi} = \boldsymbol{f}, & x \in \Omega, \quad t = 0, \end{cases} \tag{3.2}$$

where $\boldsymbol{g}_0$ and $\boldsymbol{g}_N$ are, respectively, the data corresponding to the left and right boundaries.

3.1 Definitions

Before we start analyzing problem (3.2), some definitions are needed.

Let $\boldsymbol{u}, \boldsymbol{v} \in L^2[0,1]$, where $\boldsymbol{u} = \left[u^{(1)}, u^{(2)}\right]^T$, $\boldsymbol{v} = \left[v^{(1)}, v^{(2)}\right]^T$ are complex-valued vector functions with 2 components, and let $\boldsymbol{u}^*$ denote the Hermitian transpose of $\boldsymbol{u}$. Let the inner product be defined by $(\boldsymbol{u}, \boldsymbol{v}) = \int_0^1 \boldsymbol{u}^*\boldsymbol{v}\, dx$, and let the corresponding norm be $||\boldsymbol{u}||^2 = (\boldsymbol{u}, \boldsymbol{u})$. The domain $\Omega = [0,1]$ is discretized with an equidistant grid $\{x_i\}_{i=0}^N$, such that

$$x_i = ih, \quad i = 0, 1, ..., N, \quad h = \frac{1}{N}.$$

The approximate solution at gridpoint x_i is a (2×1) vector $\boldsymbol{v}_i = \left[v_i^{(1)}, v_i^{(2)}\right]^T$ and the discrete solution vector is

$$\boldsymbol{v} = \left[v_0^{(1)}, v_1^{(1)}, ..., v_N^{(1)}, v_0^{(2)}, ..., v_N^{(2)}\right]^T_{2(N+1)\times 1}.$$

Mimicking the inner product for continuous functions, we define an inner product for discrete complex-valued vector functions, $\psi, \phi \in \mathbb{C}^{2\times(N+1)}$ by $(\psi, \phi)_H = \psi^* H\phi$, where H is Hermitian and positive definite. The corresponding norm is $||\psi||_H^2 = \psi^* H\psi$.

The following vectors will be frequently used:

$$\begin{aligned} \boldsymbol{e}_0 &= [1, 0, \ldots, 0]^T, \quad \boldsymbol{e}_N = [0, 0, \ldots, 1]^T, \\ \boldsymbol{v}_0 &= \left(I_2 \otimes \boldsymbol{e}_0^T\right)\boldsymbol{v}, \quad \boldsymbol{v}_N = \left(I_2 \otimes \boldsymbol{e}_N^T\right)\boldsymbol{v}. \end{aligned}$$

Definition 3.1. *An explicit pth-order accurate finite difference scheme with minimal stencil width of a Cauchy problem is called a pth-order accurate narrow-stencil.*

Definition 3.2. *A difference operator* $D_1 = H^{-1}Q = H^{-1}(\hat{Q} - \frac{1}{2}\boldsymbol{e}_0\boldsymbol{e}_0^T + \frac{1}{2}\boldsymbol{e}_N\boldsymbol{e}_N^T)$ *approximating* $\partial/\partial x$*, using a pth-order accurate narrow-stencil, is said to be a pth-order accurate first-derivative SBP operator if* H *is symmetric and positive definite, and* $\hat{Q} + \hat{Q}^T = 0$.

To make the notation for systems of equations more compact we introduce the Kronecker product,

$$C \otimes D = \begin{bmatrix} c_{0,0}D & \cdots & c_{0,q-1}D \\ \vdots & & \vdots \\ c_{p-1,0}D & \cdots & c_{p-1,q-1}D \end{bmatrix},$$

where C is a $p \times q$ matrix and D is an $r \times s$ matrix. The following properties of the Kronecker product will be used

- $(C \otimes D)(O \otimes P) = (CO) \otimes (DP)$, whenever CO and DP are defined;
- $(C \otimes D)^{-1} = (C^{-1} \otimes D^{-1})$, whenever C^{-1} and D^{-1} exist;
- $(C \otimes D)^* = C^* \otimes D^*$;
- if C and P are HPSD and O is HNSD, then $(C \otimes P)$ is HPSD and $(C \otimes O)$ is HNSD.

Throughout, we let I_n denote the $n \times n$ identity matrix.

3.2 Continuous analysis

Consider the case of a free particle in space, that is, when $V_0 = 0$ in (3.2). The problem becomes

$$\begin{cases} \boldsymbol{\psi}_t + A\boldsymbol{\psi}_x = 0, & x \in \Omega, \quad t > 0, \\ A_+\boldsymbol{\psi} = A_+\boldsymbol{g}_0(t), & x = 0, \quad t \geq 0, \\ A_-\boldsymbol{\psi} = A_-\boldsymbol{g}_N(t), & x = 1, \quad t \geq 0, \\ \boldsymbol{\psi} = \boldsymbol{f}, & x \in \Omega, \quad t = 0. \end{cases} . \tag{3.3}$$

Integrating by parts $(\boldsymbol{\psi}, \boldsymbol{\psi}_t)$, we get

$$(\boldsymbol{\psi}, \boldsymbol{\psi}_t) = (\boldsymbol{\psi}, -A\boldsymbol{\psi}_x) = -\left.\boldsymbol{\psi}^T A\boldsymbol{\psi}\right|_{x=0}^{x=1} + (\boldsymbol{\psi}_x, A\boldsymbol{\psi}) . \tag{3.4}$$

Also, as A is Hermitian, we have

$$(\boldsymbol{\psi}_t, \boldsymbol{\psi}) = (-A\boldsymbol{\psi}_x, \boldsymbol{\psi}) = -(\boldsymbol{\psi}_x, A\boldsymbol{\psi}) . \tag{3.5}$$

Adding expressions (3.4) and (3.5), we arrive at

$$\underbrace{(\boldsymbol{\psi}, \boldsymbol{\psi}_t) + (\boldsymbol{\psi}_t, \boldsymbol{\psi})}_{= \frac{d}{dt}\|\boldsymbol{\psi}\|^2} = -\left.\boldsymbol{\psi}^* A\boldsymbol{\psi}\right|_{x=0}^{x=1} = -\left.(\boldsymbol{\psi}^* A_+\boldsymbol{\psi} + \boldsymbol{\psi}^* A_-\boldsymbol{\psi})\right|_{x=0}^{x=1} , \tag{3.6}$$

where $\|\boldsymbol{\psi}\|^2$ is the probability of finding the particle anywhere in the domain. This quantity can also be interpreted as the mathematical energy of the system. Thus, the left-hand side of (3.6) corresponds to the rate of change of energy.

Expanding (3.6) according to the Steger-Warming flux splitting and bearing in mind the ingoing characteristic boundary conditions set in (3.3), we obtain the following energy estimate

$$\frac{d}{dt}\|\boldsymbol{\psi}\|^2 = \underbrace{\boldsymbol{\psi}^* A_-\boldsymbol{\psi}|_{x=0} - \boldsymbol{\psi}^* A_+\boldsymbol{\psi}|_{x=1}}_{\leq 0} - \underbrace{\boldsymbol{g}_N^* A_-\boldsymbol{g}_N}_{\text{known data}} + \underbrace{\boldsymbol{g}_0^* A_+\boldsymbol{g}_0}_{\text{known data}} . \tag{3.7}$$

Integrating (3.7) in time, we finally arrive at

$$\|\boldsymbol{\psi}(\cdot,t)\|^2 \leq \|\boldsymbol{\psi}(\cdot,0)\|^2 + \int_0^t \boldsymbol{g}_0^* A_+ \boldsymbol{g}_0 - \boldsymbol{g}_N^* A_- \boldsymbol{g}_N \, d\tau. \tag{3.8}$$

Hence the energy grows only in terms of known data so, for the case of a free particle, assuming the existence of a solution and bearing in mind that its uniqueness is easily proven using (3.8), problem (3.3) is strongly well posed.

3.3 Semi-discrete analysis

Discretizing the system of PDEs in (3.3) in space with the SBP–SAT method leads to the semi-discrete problem for the particle in 1-D

$$\boldsymbol{v_t} = -\underbrace{AI_2 \otimes D_1}_{\text{SBP}} \boldsymbol{v} + \underbrace{\tau_0 A_+ \otimes H^{-1}\boldsymbol{e}_0(\boldsymbol{v}_0 - \boldsymbol{g}_0)}_{\text{SAT at } x=0} + \underbrace{\tau_N A_- \otimes H^{-1}\boldsymbol{e}_N(\boldsymbol{v}_N - \boldsymbol{g}_N)}_{\text{SAT at } x=1}, \tag{3.9}$$

where τ_0 and τ_N are penalty parameters yet to be determined.

The undermentioned definition characterizes discretization methods that do not allow nonphysical solution growth in time.

Definition 3.3. *A semi-discretization is said to be strictly stable if the solution growth rate of the discrete problem is bounded by the growth rate of the (well-posed) continuous problem.*

In the following lemma, we present penalty parameters that yield a strictly stable semi-discretization.

Lemma 3.1. *The scheme* (3.9) *is strictly stable if* $\tau_0 = -1$ *and* $\tau_N = 1$.

Proof. Multiplying (3.9) by $\boldsymbol{v}^*(I_2 \otimes H)$ and then adding the conjugate transpose leads to

$$\begin{aligned}
\frac{d}{dt}||\boldsymbol{v}||_H^2 &= (\boldsymbol{v}, \boldsymbol{v}_t)_H + (\boldsymbol{v}_t, \boldsymbol{v})_H = \boldsymbol{v}^*(I_2 \otimes H)\boldsymbol{v}_t + \boldsymbol{v}_t^*(I_2 \otimes H)v \\
&= -\boldsymbol{v}^* \underbrace{\left(A \otimes (\hat{Q} + \hat{Q}^*)\right)}_{=0} v + \boldsymbol{v}_0^* A \boldsymbol{v}_0 - \boldsymbol{v}_N^* A \boldsymbol{v}_N \\
&\quad + \tau_0 \boldsymbol{v}_0^* A_+(\boldsymbol{v}_0 - \boldsymbol{g}_0) + \tau_N \boldsymbol{v}_N^* A_-(\boldsymbol{v}_N - \boldsymbol{g}_N) \\
&\quad + \tau_0^*(\boldsymbol{v}_0 - \boldsymbol{g}_0)^* A_+ \boldsymbol{v}_0 + \tau_N^*(\boldsymbol{v}_N - \boldsymbol{g}_N)^* A_- \boldsymbol{v}_N.
\end{aligned}$$

Choosing the penalty parameters such that $\tau_0 = -1$ and $\tau_N = 1$, we finally arrive at

$$\begin{aligned}
\frac{d}{dt}||\boldsymbol{v}||_H^2 &= \boldsymbol{v}_0^* A_- \boldsymbol{v}_0 - \boldsymbol{v}_N^* A_+ \boldsymbol{v}_N - \boldsymbol{g}_N^* A_- \boldsymbol{g}_N + \boldsymbol{g}_0^* A_+ \boldsymbol{g}_0 \\
&\quad \underbrace{-(\boldsymbol{v}_0 - \boldsymbol{g}_0)^* A_+(\boldsymbol{v}_0 - \boldsymbol{g}_0) + (\boldsymbol{v}_N - \boldsymbol{g}_N)^* A_-(\boldsymbol{v}_N - \boldsymbol{g}_N)}_{\text{damping terms} \leq 0},
\end{aligned}$$

which is analogous to the continuous energy estimate (3.8), with the addition of two damping terms that vanish with grid refinement. Therefore, the discrete solution growth rate is bounded by the continuous growth rate, and hence the scheme (3.9) is strictly stable. □

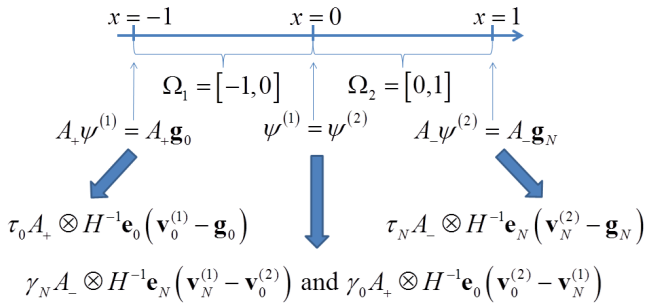

Figure 2: Relation between the physical domain with a potential barrier and the SAT terms.

3.3.1 1-D Interface treatment

In order to introduce a barrier, we now consider our domain to be $\Omega = [-1,1] = \Omega_1 \cup \Omega_2$, with $\Omega_1 = [-1,0]$ and $\Omega_2 = [0,1]$, as illustrated in Figure 2.

The potential barrier will be introduced in Ω_2, while in Ω_1 the particle is still free. Thus, the problem we are considering takes the form

$$\begin{cases} \boldsymbol{\psi}_t^{(1)} + A\boldsymbol{\psi}_x^{(1)} = 0, & x \in \Omega_1, \quad t > 0, \\ \boldsymbol{\psi}_t^{(2)} + A\boldsymbol{\psi}_x^{(2)} = -(i/\hbar)V_0\boldsymbol{\psi}^{(2)}, & x \in \Omega_2, \quad t > 0, \\ A_-\boldsymbol{\psi} = A_-\boldsymbol{g}_N(t), & x = 1, \quad t \geq 0, \\ A_+\boldsymbol{\psi} = A_+\boldsymbol{g}_0(t), & x = -1, \quad t \geq 0, \\ \boldsymbol{\psi} = \boldsymbol{f}, & x \in \Omega, \quad t = 0, \end{cases} \tag{3.10}$$

where $\boldsymbol{\psi}^{(1)}$ and $\boldsymbol{\psi}^{(2)}$ denote the solutions in Ω_1 and Ω_2, respectively.

Moreover, for our solution to make physical sense, it has to be continuous across the interface between Ω_1 and Ω_2, that is, we have to impose

$$\boldsymbol{\psi}^{(1)} = \boldsymbol{\psi}^{(2)}, \quad x = 0. \tag{3.11}$$

For the sake of notational simplicity, assuming the same number of grid points in the spatial discretization of each subdomain, a semi-discrete approximation of (3.10) is given by

$$\begin{cases} \boldsymbol{v}_t^{(1)} = -AI_2 \otimes D_1\boldsymbol{v}^{(1)} + \\ \qquad + \tau_0 A_+ \otimes H^{-1}\boldsymbol{e}_0\left(\boldsymbol{v}_0^{(1)} - \boldsymbol{g}_0\right) + \gamma_N A_- \otimes H^{-1}\boldsymbol{e}_N\left(\boldsymbol{v}_N^{(1)} - \boldsymbol{v}_0^{(2)}\right), \\ \boldsymbol{v}_t^{(2)} = -AI_2 \otimes D_1\boldsymbol{v}^{(2)} - (i/\hbar)\boldsymbol{v}_0\boldsymbol{v}^{(2)} \\ \qquad + \tau_N A_- \otimes H^{-1}\boldsymbol{e}_N\left(\boldsymbol{v}_N^{(2)} - \boldsymbol{g}_N\right) + \gamma_0 A_+ \otimes H^{-1}\boldsymbol{e}_0\left(\boldsymbol{v}_0^{(2)} - \boldsymbol{v}_N^{(1)}\right). \end{cases} \tag{3.12}$$

Lemma 3.2. *The scheme* (3.12) *is strictly stable if* $\tau_0 = -1 = \gamma_0$, $\tau_N = 1 = \gamma_N$.

Proof. We start by setting $\tau_0 = -1$, $\tau_N = 1$, $\gamma_0 = -1$ and $\gamma_N = 1$ and then multiply the first and second equations in (3.12) by ${v^{(1)}}^* I_2 \otimes H$ and ${v^{(2)}}^* I_2 \otimes H$,

respectively. Then, adding the conjugate transpose, we arrive at the following discrete energy estimate

$$\begin{aligned}
\frac{d}{dt}\left(||\boldsymbol{v}^{(1)}||_H^2 + ||\boldsymbol{v}^{(2)}||_H^2\right) &= (\boldsymbol{v}^{(1)}, \boldsymbol{v}_t^{(1)})_H + (, \boldsymbol{v}_t^{(1)}, \boldsymbol{v}^{(1)})_H \\
&\quad + (\boldsymbol{v}^{(2)}, \boldsymbol{v}_t^{(2)})_H + (, \boldsymbol{v}_t^{(2)}, \boldsymbol{v}^{(2)})_H \\
&= \boldsymbol{v}^{(1)^*} I_2 \otimes H \boldsymbol{v}_t^{(1)} + \boldsymbol{v}_t^{(1)^*} I_2 \otimes H \boldsymbol{v}^{(1)} + \\
&\quad + \boldsymbol{v}^{(2)^*} I_2 \otimes H \boldsymbol{v}_t^{(2)} + \boldsymbol{v}_t^{(2)^*} I_2 \otimes H \boldsymbol{v}^{(2)} \\
&= -\left(\boldsymbol{v}^{(1)} + \boldsymbol{v}^{(2)}\right)^* \underbrace{(A \otimes (Q + Q^*))}_{=0} \left(\boldsymbol{v}^{(1)} + \boldsymbol{v}^{(2)}\right) \\
&\quad \underbrace{-(i/\hbar)\boldsymbol{v}_0 v^{(2)^*} I_2 \otimes H + (i/\hbar)\boldsymbol{v}_0 v^{(2)^*} I_2 \otimes H}_{=0} \\
&\quad + \boldsymbol{v}_0^{(1)^*} A_- \boldsymbol{v}_0^{(1)} - \left(\boldsymbol{v}_0^{(1)} - \boldsymbol{g}_0\right)^* A_+ \left(\boldsymbol{v}_0^{(1)} - \boldsymbol{g}_0\right) + \boldsymbol{g}_0^* A_+ \boldsymbol{g}_0 \\
&\quad - \boldsymbol{v}_N^{(2)^*} A_+ \boldsymbol{v}_N^{(2)} + \left(\boldsymbol{v}_N^{(2)} - \boldsymbol{g}_N\right)^* A_- \left(\boldsymbol{v}_N^{(2)} - \boldsymbol{g}_N\right) - \boldsymbol{g}_N^* A_+ \boldsymbol{g}_N \\
&\quad + \left(\boldsymbol{v}_N^{(1)} - \boldsymbol{v}_0^{(2)}\right)^* (A_- - A_+) \left(\boldsymbol{v}_N^{(1)} - \boldsymbol{v}_0^{(2)}\right).
\end{aligned}$$

Thus, this case is analogous to the discrete energy estimate for the free particle case, except for the interface contribution $\left(\boldsymbol{v}_N^{(1)} - \boldsymbol{v}_0^{(2)}\right)^* (A_- - A_+) \left(\boldsymbol{v}_N^{(1)} - \boldsymbol{v}_0^{(2)}\right)$ which is a damping term that vanishes with grid refinement, since $(A_- - A_+)$ is HNSD. Therefore, the multi-block discretization (3.12) is strictly stable. □

3.4 Convergence study

The convergence study is performed in a single-block domain with no potential barrier, using the analytical plane wave solution derived in Section 2.1 as a reference solution. Since these simulations are performed only in 1-D, $k^{(2)}$ is set to zero in the analytical solution. The analytical solution is used as initial data.

For each refinement of the grid, the error is analyzed at $t = 5 \cdot 10^{-14}$, that is, at the 500th time step, with a fixed time step size of $k = 10^{-16}$ s, conservatively below the requirements of the CFL condition.

We now compute the error convergence rate q, which is defined in [2] as:

$$q = \frac{\log_{10}\left(\frac{||v_{ref} - v^{(N_2)}||_h}{||v_{ref} - v^{(N_1)}||_h}\right)}{\log_{10}\left(\frac{N_1}{N_2}\right)}, \tag{3.13}$$

where $||v||_h = \sqrt{h \sum_j v_j^2}$ and the reference solution, v_{ref}, is the analytical solution derived in Section 2.1. The magnitude of the error and the results of the error convergence analysis are presented in Table 1. It is seen that the method asymptotically reaches the expected overall error convergence rates, $p + 1$ for an SBP operator of order $2p$, which was theoretically expected.

Table 1: Error and error convergence rates, according to Eq. 3.13, for SBP operators with different orders of accuracy. Note that the global convergence rate asymptotically approaches $p+1$ for an SBP operator of order $2p$. N is the number of grid points in the domain, whose length is 500 nm.

N	2nd	$q^{(2)}$	4th	$q^{(4)}$	6th	$q^{(6)}$
101	3.56e-04		3.37e-05		3.94e-05	
201	9.01e-05	2.00	3.09e-06	3.47	3.05e-06	3.72
401	2.26e-05	2.01	3.36e-07	3.21	2.00e-07	3.94
801	5.64e-06	2.00	4.01e-08	3.07	1.26e-08	3.99
N	8th	$q^{(8)}$	10th	$q^{(10)}$		
101	2.60e-05		3.98e-05			
201	8.95e-07	4.89	7.44e-07	5.78		
401	2.66e-08	5.09	1.23e-08	5.94		
801	8.24e-10	5.02	1.96e-10	5.99		

3.5 Simulations of Klein-tunneling

In a physical sense, it is more realistic to let a wave-packet travel towards the potential barrier than to use a plane wave solution. In order to create the initial conditions of the simulations, the plane wave solution is used with a Gaussian envelope. The initial conditions for the simulations then become

$$\boldsymbol{\psi}(x,0) = \begin{bmatrix} 1 \\ 1 \end{bmatrix} e^{i(kx-\nu_F kt)} \cdot e^{-\frac{x^2}{4\sigma}}, \tag{3.14}$$

where the last term creates a Gaussian envelope, and σ is a measure of its width. In this case, the characteristic boundary conditions are set to zero, that is $\boldsymbol{g}_0 = \boldsymbol{g}_N = 0$, in order to create non-reflecting boundary conditions.

Since $\boldsymbol{\psi}$ is a two component complex spinor function, the representation of the solution, in Figure 3, is done only for the real part of the first component, on the left column. $\boldsymbol{\psi}^*\boldsymbol{\psi}$, which is often interpreted as the probability density function, is shown on the right column.

As expected from the theoretical results, the 1-D case is similar to a particle traveling perpendicularly towards the potential barrier, which means that the particle would travel through the barrier with absolute certainty. This phenomenon, which, as mentioned earlier, is called Klein-tunneling, can be seen from Figure 3, where the shape of the probability density function remains the same and, as observed in our numerical experiments, would remain so, regardless of the height or width of the potential barrier. Regarding the grid resolution, we have used about 40 grid points per wavelength in this case, which is more than enough to make discretization errors negligible. Another observation that can be made from looking at Figure 3 is that the frequency of the components increase within the barrier. Our observations also indicate that the higher the potential within the barrier, the more the frequency increases, which in extreme cases creates a requirement for a finer grid within the barrier.

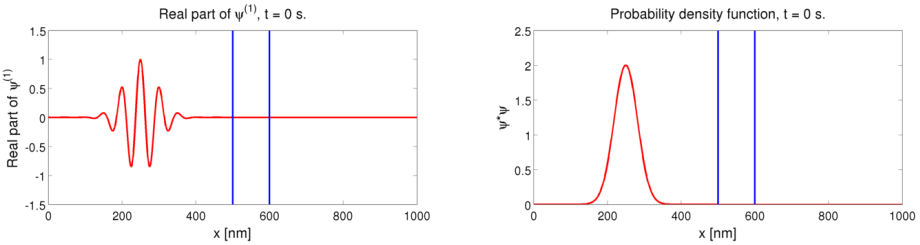

(a) Initial condition

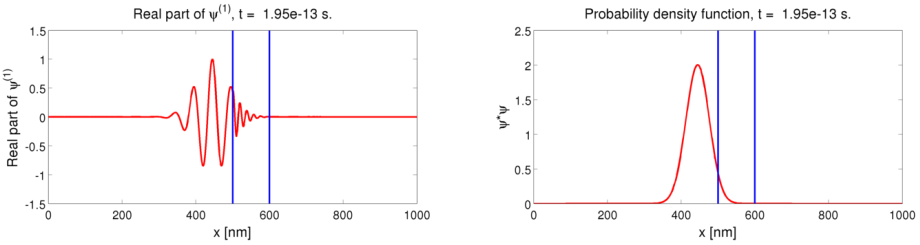

(b) $t = 1.95 \cdot 10^{-13}$ s

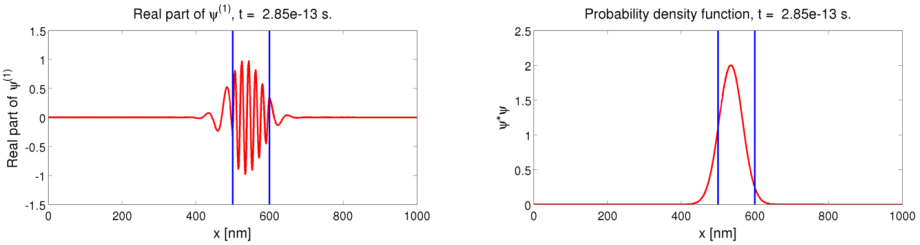

(c) $t = 2.85 \cdot 10^{-13}$ s

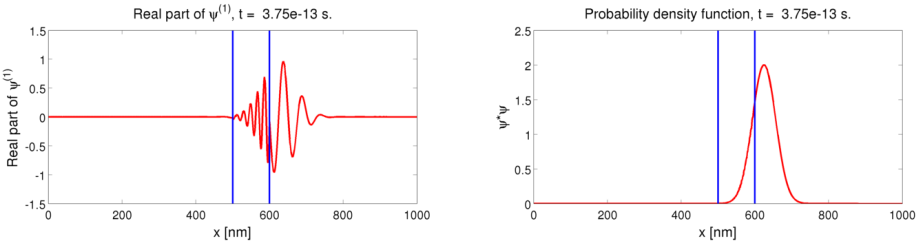

(d) $t = 3.75 \cdot 10^{-13}$ s

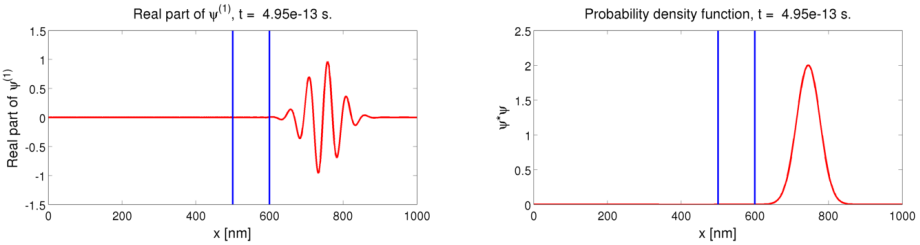

(e) $t = 4.95 \cdot 10^{-13}$ s

Figure 3: To the right: a non-normalized probability density function simulating a massless fermion of energy 80 meV traveling in single-layer graphene towards a barrier of 300 meV. To the left: the corresponding real part of the first component of the spinor. Note that the frequency of the components increases within the barrier, while the shape of the probability function remains the same.

4 The 2-D Problem

In two dimensions, the equation describing massless Dirac fermions in single-layer graphene can be written

$$\boldsymbol{\psi}_t + A\boldsymbol{\psi}_x + B\boldsymbol{\psi}_y = -(i/\hbar)V_0\boldsymbol{\psi}. \tag{4.1}$$

Considering the domain to be the unit square

$$\Omega_{0,0}^{1,1} = \left\{(x,y) \in \mathbb{R}^2 : 0 \le x \le 1\,; 0 \le y \le 1\right\}$$

and bearing in mind the Steger-Warming flux splitting defined in Section 2.2, we can impose boundary conditions on the ingoing characteristic variables by specifying $A_+\boldsymbol{\psi}$ and $A_-\boldsymbol{\psi}$ at the west (W) and east (E) boundaries, and $B_+\boldsymbol{\psi}$ and $B_-\boldsymbol{\psi}$ at the south (S) and north (N) boundaries, respectively. We then obtain the following 2-D problem

$$\begin{cases} \boldsymbol{\psi}_t + A\boldsymbol{\psi}_x + B\boldsymbol{\psi}_y = -(i/\hbar)V_0\boldsymbol{\psi}, & \boldsymbol{r} \in \Omega_{0,0}^{1,1}, \quad t > 0, \\ A_+\boldsymbol{\psi} = A_+\boldsymbol{g}_W(y,t) & \boldsymbol{r} \in W, \quad t \ge 0, \\ A_-\boldsymbol{\psi} = A_-\boldsymbol{g}_E(y,t) & \boldsymbol{r} \in E, \quad t \ge 0, \\ B_+\boldsymbol{\psi} = B_+\boldsymbol{g}_S(x,t) & \boldsymbol{r} \in S, \quad t \ge 0, \\ B_-\boldsymbol{\psi} = B_-\boldsymbol{g}_N(x,t) & \boldsymbol{r} \in N, \quad t \ge 0, \\ \boldsymbol{\psi} = \boldsymbol{f}, & \boldsymbol{r} \in \Omega_{0,0}^{1,1}, \quad t = 0, \end{cases} \tag{4.2}$$

where $\boldsymbol{g}_W, \boldsymbol{g}_E, \boldsymbol{g}_S$ and $\boldsymbol{g}_N$ are, respectively, the data corresponding to the east, west, south and north boundaries.

4.1 Definitions

Before we start solving Equation (4.2) some definitions are needed.

Let $\boldsymbol{u}, \boldsymbol{v} \in L^2[\Omega_{e,s}^{w,n}]$ where $\boldsymbol{u} = [u^{(1)}, u^{(2)}]^T$ and $\boldsymbol{v} = [v^{(1)}, v^{(2)}]^T$ are complex-valued vector functions with 2 components. Let the inner product be defined by $(\boldsymbol{u}, \boldsymbol{v}) = \int_e^w \int_s^n \boldsymbol{u}^* \boldsymbol{v} dx$, and let the corresponding norm be $||\boldsymbol{u}||^2 = (\boldsymbol{u}, \boldsymbol{u})$.

Let $\boldsymbol{r} = (x, y)$ denote the position vector in two dimensions and consider the computational domain $\Omega_{e,s}^{w,n} = \left\{(x,y) \in \mathbb{R}^2 : w \le x \le e\,; s \le y \le n\right\}$. This domain is discretized using an $(N_x+1) \times (N_y+1)$-point equidistant grid defined as:

$$x_i = w + ih_x,\ i = 0, 1, \ldots, N_x, \quad h_x = \frac{e-w}{N_x},$$

$$y_j = s + jh_y,\ i = 0, 1, \ldots, N_y, \quad h_y = \frac{n-s}{N_y}.$$

In order to simplify the notation, we take $N_x = N_y = N - 1$. The approximate solution at the grid point (x_i, y_j) is $\boldsymbol{v}_{i,j} = \begin{bmatrix} v_{i,j}^{(1)} \\ v_{i,j}^{(2)} \end{bmatrix}$ and, for computational purposes, the entire solution vector should be defined as

$$\boldsymbol{v} = \left[v_{00}^{(1)}, \ldots, v_{0N_y}^{(1)}, v_{10}^{(1)}, \ldots, v_{1N_y}^{(1)}, \ldots, v_{N_xN_y}^{(1)}, \ldots, v_{00}^{(2)}, \ldots, v_{0N_y}^{(2)}, \ldots, v_{N_xN_y}^{(2)}\right]_{1\times 2N^2}.$$

To distinguish whether a 2-D difference operator R is operating in the x- or the y-direction, we use the notations R_x and R_y, respectively. The following

2-D operators will be used:

$$
\begin{array}{ll}
D_x = I_2 \otimes D_1 \otimes I_N, & D_y = I_2 \otimes I_N \otimes D_1, \\
H_x = I_2 \otimes H \otimes I_N, & H_y = I_2 \otimes I_N \otimes H, \\
E_W = I_2 \otimes \boldsymbol{e}_0 \otimes I_N, & E_S = I_2 \otimes I_N \otimes \boldsymbol{e}_0, \\
E_E = I_2 \otimes \boldsymbol{e}_N \otimes I_N, & E_N = I_2 \otimes I_N \otimes \boldsymbol{e}_N, \\
\tilde{H} = H_x H_y = I_2 \otimes H \otimes H, &
\end{array}
$$

where we refer to the 4 boundaries of the domain as W (West), E (East), S (South) and N (North) boundaries, D_1 and H are the 1-D operators introduced earlier, and $\boldsymbol{e}_0$ and $\boldsymbol{e}_N$ are the 1-D "boundary" vectors defined earlier. Note that the matrix E_W is defined so that $\boldsymbol{v}_W = E_W^* \boldsymbol{v}$ is a vector that contains only the elements of $\boldsymbol{v}$ that correspond to the west boundary. The matrices E_E, E_S and E_N, and respective vectors $\boldsymbol{v}_E$, $\boldsymbol{v}_S$ and $\boldsymbol{v}_N$, are defined in a similar way for each of the other boundaries.

4.2 Continuous analysis

Consider the case of a free particle in 2-D space, that is, when $V_0 = 0$ in (4.2), by solving

$$
\begin{cases}
\boldsymbol{\psi}_t + A\boldsymbol{\psi}_x + B\boldsymbol{\psi}_y = 0, & \boldsymbol{r} \in \Omega_{0,0}^{1,1}, \quad t > 0, \\
A_+\boldsymbol{\psi} = A_+ \boldsymbol{g}_W(y,t), & \boldsymbol{r} \in W, \quad t \geq 0, \\
A_-\boldsymbol{\psi} = A_- \boldsymbol{g}_E(y,t), & \boldsymbol{r} \in E, \quad t \geq 0, \\
B_+\boldsymbol{\psi} = B_+ \boldsymbol{g}_S(x,t), & \boldsymbol{r} \in S, \quad t \geq 0, \\
B_-\boldsymbol{\psi} = B_- \boldsymbol{g}_N(x,t), & \boldsymbol{r} \in N, \quad t \geq 0, \\
\boldsymbol{\psi} = \boldsymbol{f}, & \boldsymbol{r} \in \Omega_{0,0}^{1,1}, \quad t = 0,
\end{cases}
\tag{4.3}
$$

Multiplying the first equation in problem (4.3) by $\boldsymbol{\psi}^*$, adding the transpose and integrating over the domain $\Omega_{0,0}^{1,1}$ results in the following energy estimate

$$
\begin{aligned}
\frac{d}{dt}||\boldsymbol{\psi}||^2 &= \int_\Omega \boldsymbol{\psi}^* \boldsymbol{\psi}_t + \boldsymbol{\psi}_t^* \boldsymbol{\psi} d\Omega \\
&= -\int_\Omega \frac{\partial}{\partial x}\left(\boldsymbol{\psi}^* A \boldsymbol{\psi}\right) d\Omega - \int_\Omega \frac{\partial}{\partial y}\left(\boldsymbol{\psi}^* B \boldsymbol{\psi}\right) d\Omega \\
&= \underbrace{\int_W \boldsymbol{\psi}^* A \boldsymbol{\psi} dy}_{=BT_W} \underbrace{- \int_E \boldsymbol{\psi}^* A \boldsymbol{\psi} dy}_{=BT_E} + \underbrace{\int_S \boldsymbol{\psi}^* B \boldsymbol{\psi} dx}_{=BT_S} \underbrace{\int_N \boldsymbol{\psi}^* B \boldsymbol{\psi} dx}_{=BT_N} \\
&= BT_W + BT_E + BT_S + BT_N
\end{aligned}
\tag{4.4}
$$

where the boundary terms are

$$
BT_W = \underbrace{\int_W \boldsymbol{\psi}^* A_+ \boldsymbol{\psi} dy}_{=\int_W \boldsymbol{g}_W^* A_+ \boldsymbol{g}_W dy} + \underbrace{\int_W \boldsymbol{\psi}^* A_- \boldsymbol{\psi} dy}_{\leq 0}, \quad BT_E = \underbrace{-\int_E \boldsymbol{\psi}^* A_+ \boldsymbol{\psi} dy}_{\leq 0} \underbrace{- \int_E \boldsymbol{\psi}^* A_- \boldsymbol{\psi} dy}_{=-\int_E \boldsymbol{g}_E^* A_- \boldsymbol{g}_E dy},
$$

$$
BT_S = \underbrace{\int_S \boldsymbol{\psi}^* B_+ \boldsymbol{\psi} dx}_{=\int_S \boldsymbol{g}_S^* B_+ \boldsymbol{g}_S dx} + \underbrace{\int_S \boldsymbol{\psi}^* B_- \boldsymbol{\psi} dx}_{\leq 0}, \quad BT_N = \underbrace{-\int_N \boldsymbol{\psi}^* B_+ \boldsymbol{\psi} dx}_{\leq 0} \underbrace{- \int_N \boldsymbol{\psi}^* B_- \boldsymbol{\psi} dx}_{=-\int_N \boldsymbol{g}_N^* B_- \boldsymbol{g}_N dx}.
$$

Thus

$$\frac{d}{dt}||\boldsymbol{\psi}(r,t)||^2 \leq \underbrace{\int_W \boldsymbol{g}_W^* A_+ \boldsymbol{g}_W dy}_{=I_{W+}} - \underbrace{\int_E \boldsymbol{g}_E^* A_- \boldsymbol{g}_E dy}_{=I_{E-}} + \underbrace{\int_S \boldsymbol{g}_S^* B_+ \boldsymbol{g}_S dx}_{I_{S+}} - \underbrace{\int_N \boldsymbol{g}_N^* B_- \boldsymbol{g}_N dx}_{I_{N-}}.$$

Integrating the last expression in time, we finally arrive at

$$||\boldsymbol{\psi}(\cdot,t)||^2 \leq ||\boldsymbol{\psi}(\cdot,0)||^2 + \int_0^t \left(I_{W+} - I_{E-} + I_{S+} - I_{N-}\right) d\tau. \tag{4.5}$$

Hence we obtain an energy growth only in terms of known data so, for the case of a free particle, assuming the existence of a solution and bearing in mind that its uniqueness is easily proven using (4.5), problem (4.3) is strongly well posed.

4.3 Semi-discrete analysis

Discretizing the system of PDEs in (4.3) in space with the SBP–SAT method leads to the semi-discrete problem for a free particle in 2-D

$$\boldsymbol{v_t} = -AD_x\boldsymbol{v} - BD_y\boldsymbol{v} + SAT, \tag{4.6}$$

where $SAT = SAT_W + SAT_E + SAT_S + SAT_N$ is the sum of the SAT terms from each boundary

$$\begin{aligned}
SAT_W &= -\left(A_+ \otimes H^{-1}\boldsymbol{e}_0 \otimes I_N\right)(\boldsymbol{v}_W - \boldsymbol{g}_W),\\
SAT_E &= \left(A_- \otimes H^{-1}\boldsymbol{e}_N \otimes I_N\right)(\boldsymbol{v}_E - \boldsymbol{g}_E),\\
SAT_S &= -\left(B_+ \otimes I_N \otimes H^{-1}\boldsymbol{e}_0\right)(\boldsymbol{v}_S - \boldsymbol{g}_S),\\
SAT_N &= \left(B_- \otimes I_N \otimes H^{-1}\boldsymbol{e}_N\right)(\boldsymbol{v}_N - \boldsymbol{g}_N).
\end{aligned}$$

In the following lemma, we prove the strict stability of the suggested semi-discretization.

Lemma 4.1. *The scheme* (4.6) *is strictly stable.*

Proof. We first multiply (4.6) by $\boldsymbol{v}^*\tilde{H}$ and then add the conjugate transpose, obtaining

$$\begin{aligned}
\frac{d}{dt}\|v\|_{\tilde{H}}^2 &= \boldsymbol{v}^*\tilde{H}\boldsymbol{v}_t + \boldsymbol{v}_t^*\tilde{H}v\\
&= -\boldsymbol{v}^*\tilde{H}(AD_x + BD_y)\boldsymbol{v} + \boldsymbol{v}^*\tilde{H}(SAT_W) + \boldsymbol{v}^*\tilde{H}(SAT_E) + \boldsymbol{v}^*\tilde{H}(SAT_S) + \boldsymbol{v}^*\tilde{H}(SAT_N)\\
&\quad - \boldsymbol{v}^*(AD_x + BD_y)^*\tilde{H}\boldsymbol{v} + (SAT_W)^*\tilde{H}\boldsymbol{v} + (SAT_E)^*\tilde{H}\boldsymbol{v} + (SAT_S)^*\tilde{H}\boldsymbol{v} + (SAT_N)^*\tilde{H}\boldsymbol{v}\\
&= BT_W + BT_E + BT_S + BT_N
\end{aligned}$$

where

$$
\begin{aligned}
BT_W &= \boldsymbol{v}_W^* \left(A_- \otimes H\right) \boldsymbol{v}_W + \boldsymbol{v}_W^* \left(A_+ \otimes H\right) \boldsymbol{g}_W - \left(\boldsymbol{v}_W - \boldsymbol{g}_W\right)^* \left(A_+ \otimes H\right) \boldsymbol{v}_W \\
&= \underbrace{\boldsymbol{v}_W^* \left(A_- \otimes H\right) \boldsymbol{v}_W}_{\leq 0} + \underbrace{\boldsymbol{g}_W^* \left(A_+ \otimes H\right) \boldsymbol{g}_W}_{\text{known data}} \underbrace{-\left(\boldsymbol{v}_W - \boldsymbol{g}_W\right)^* \left(A_+ \otimes H\right) \left(\boldsymbol{v}_W - \boldsymbol{g}_W\right)}_{\leq 0;\quad \text{damping term}};
\end{aligned}
$$

$$
\begin{aligned}
BT_E &= -\boldsymbol{v}_E^* \left(A_+ \otimes H\right) \boldsymbol{v}_E - \boldsymbol{v}_E^* \left(A_- \otimes H\right) \boldsymbol{g}_E + \left(\boldsymbol{v}_E - \boldsymbol{g}_E\right)^* \left(A_- \otimes H\right) \boldsymbol{v}_E \\
&= \underbrace{-\boldsymbol{v}_E^* \left(A_+ \otimes H\right) \boldsymbol{v}_E}_{\leq 0} - \underbrace{\boldsymbol{g}_E^* \left(A_- \otimes H\right) \boldsymbol{g}_E}_{\text{known data}} \underbrace{+\left(\boldsymbol{v}_E - \boldsymbol{g}_E\right)^* \left(A_- \otimes H\right) \left(\boldsymbol{v}_E - \boldsymbol{g}_E\right)}_{\leq 0;\quad \text{damping term}};
\end{aligned}
$$

$$
\begin{aligned}
BT_S &= \boldsymbol{v}_S^* \left(B_- \otimes H\right) \boldsymbol{v}_S + \boldsymbol{v}_S^* \left(B_+ \otimes H\right) \boldsymbol{g}_S - \left(\boldsymbol{v}_S - \boldsymbol{g}_S\right)^* \left(B_+ \otimes H\right) \boldsymbol{v}_S \\
&= \underbrace{\boldsymbol{v}_S^* \left(B_- \otimes H\right) \boldsymbol{v}_S}_{\leq 0} + \underbrace{\boldsymbol{g}_S^* \left(B_+ \otimes H\right) \boldsymbol{g}_S}_{\text{known data}} \underbrace{-\left(\boldsymbol{v}_S - \boldsymbol{g}_S\right)^* \left(B_+ \otimes H\right) \left(\boldsymbol{v}_S - \boldsymbol{g}_S\right)}_{\leq 0;\quad \text{damping term}};
\end{aligned}
$$

$$
\begin{aligned}
BT_N &= -\boldsymbol{v}_N^* \left(B_+ \otimes H\right) \boldsymbol{v}_N - \boldsymbol{v}_N^* \left(B_- \otimes H\right) \boldsymbol{g}_N + \left(\boldsymbol{v}_N - \boldsymbol{g}_N\right)^* \left(B_- \otimes H\right) \boldsymbol{v}_N \\
&= \underbrace{-\boldsymbol{v}_N^* \left(B_+ \otimes H\right) \boldsymbol{v}_N}_{\leq 0} - \underbrace{\boldsymbol{g}_N^* \left(B_- \otimes H\right) \boldsymbol{g}_N}_{\text{known data}} \underbrace{+\left(\boldsymbol{v}_N - \boldsymbol{g}_N\right)^* \left(B_- \otimes H\right) \left(\boldsymbol{v}_N - \boldsymbol{g}_N\right)}_{\leq 0;\quad \text{damping term}}.
\end{aligned}
$$

which is analogous to the continuous energy estimate (4.4),with the addition of some damping terms that vanish with grid refinement. Therefore, the discrete solution growth rate is bounded by the continuous growth rate, and hence the scheme (4.6) is strictly stable. □

4.3.1 2-D Interface treatment

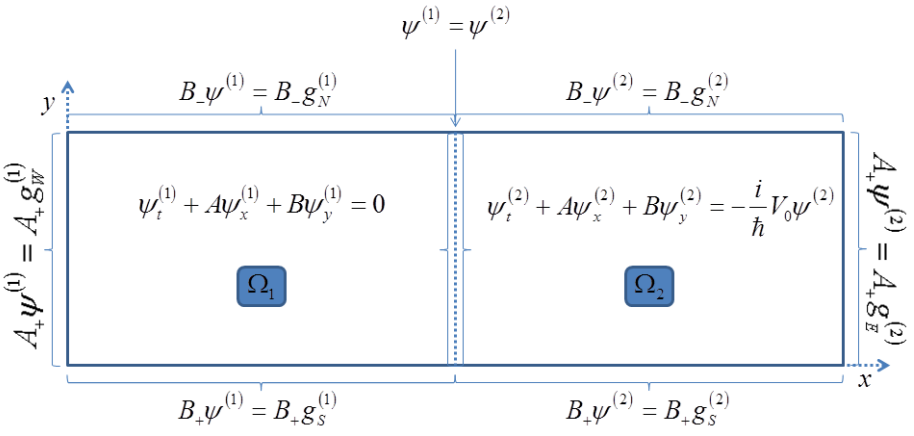

Figure 4: Illustration of the domain in consideration, composed by two 2-D blocks with different potentials, connected by an interface, and respective boundary conditions.

In order to introduce a potential barrier, one has now to consider two different blocks with different potentials, connected by an interface. See Figure 4 for an illustration of the domain and the corresponding boundary conditions.

The problem we are considering is

$$\begin{cases} \boldsymbol{\psi}_t^{(1)} + A\boldsymbol{\psi}_x^{(1)} + B\boldsymbol{\psi}_y^{(1)} = 0, & \boldsymbol{r} \in \Omega_1, & t > 0, \\ \boldsymbol{\psi}_t^{(2)} + A\boldsymbol{\psi}_x^{(2)} + B\boldsymbol{\psi}_y^{(2)} = -\frac{i}{\hbar} V_0 \boldsymbol{\psi}^{(2)}, & \boldsymbol{r} \in \Omega_2, & t > 0, \\ A_+ \boldsymbol{\psi}^{(1)} = A_+ \boldsymbol{g}_W, & \boldsymbol{r} \in W, & t > 0, \\ A_- \boldsymbol{\psi}^{(2)} = A_+ \boldsymbol{g}_E, & \boldsymbol{r} \in E, & t > 0, \\ B_+ \boldsymbol{\psi}^{(1,2)} = B_+ \boldsymbol{g}_S^{(1,2)}, & \boldsymbol{r} \in S^{(1,2)}, & t > 0, \\ B_- \boldsymbol{\psi}^{(1,2)} = B_- \boldsymbol{g}_N^{(1,2)}, & \boldsymbol{r} \in N^{(1,2)}, & t > 0, \\ \boldsymbol{\psi}^{(1)} = \boldsymbol{\psi}^{(2)}, & \boldsymbol{r} \in I, & t > 0, \\ \boldsymbol{\psi} = \boldsymbol{f}, & \boldsymbol{r} \in \Omega, & t = 0, \end{cases} \tag{4.7}$$

Note that, as in the 1-D interface treatment, for the solution to make physical sense, it has to be continuous across the interface between Ω_1 and Ω_2, that is, we have to impose

$$\boldsymbol{\psi}^{(1)} = \boldsymbol{\psi}^{(2)}, \quad \boldsymbol{r} \in I. \tag{4.8}$$

The resulting spatial semi-discretization of (4.7) is then

$$\begin{cases} \boldsymbol{v}_t^{(1)} = -AD_x \boldsymbol{v}^{(1)} - BD_y \boldsymbol{v}^{(1)} + SAT^{(1)} \\ \boldsymbol{v}_t^{(2)} = -AD_x \boldsymbol{v}^{(2)} - BD_y \boldsymbol{v}^{(2)} + \frac{i}{\hbar} V_0 \boldsymbol{v}^{(2)} + SAT^{(2)} \end{cases} \tag{4.9}$$

where the SAT terms are defined as $SAT^{(1)} = SAT_W^{(1)} + SAT_I^{(1)} + SAT_S^{(1)} + SAT_N^{(1)}$ and $SAT^{(2)} = SAT_I^{(2)} + SAT_E^{(2)} + SAT_S^{(2)} + SAT_N^{(2)}$, with

$$\begin{aligned} SAT_W^{(1)} &= -(A_+ \otimes H^{-1}\boldsymbol{e}_0 \otimes I_N)(\boldsymbol{v}_W^{(1)} - \boldsymbol{g}_W) \\ SAT_I^{(1)} &= (A_- \otimes H^{-1}\boldsymbol{e}_N \otimes I_N)(\boldsymbol{v}_I^{(1)} - \boldsymbol{v}_I^{(2)}) \\ SAT_S^{(1)} &= -(B_+ \otimes I_N \otimes H^{-1}\boldsymbol{e}_0)(\boldsymbol{v}_S^{(1)} - \boldsymbol{g}_S^{(1)}) \\ SAT_N^{(1)} &= (B_- \otimes I_N \otimes H^{-1}\boldsymbol{e}_N)(\boldsymbol{v}_N^{(1)} - \boldsymbol{g}_N^{(1)}) \\ SAT_I^{(2)} &= -(A_+ \otimes H^{-1}\boldsymbol{e}_0 \otimes I_N)(\boldsymbol{v}_I^{(2)} - \boldsymbol{v}_I^{(1)}) \\ SAT_E^{(2)} &= (A_- \otimes H^{-1}\boldsymbol{e}_N \otimes I_N)(\boldsymbol{v}_E^{(2)} - \boldsymbol{g}_E) \\ SAT_S^{(2)} &= -(B_+ \otimes I_N \otimes H^{-1}\boldsymbol{e}_0)(\boldsymbol{v}_S^{(2)} - \boldsymbol{g}_S^{(2)}) \\ SAT_N^{(2)} &= (B_- \otimes I_N \otimes H^{-1}\boldsymbol{e}_N)(\boldsymbol{v}_N^{(2)} - \boldsymbol{g}_N^{(2)}) \end{aligned}$$

The stability analysis is done by the energy method.

Lemma 4.2. *The scheme* (4.9) *is strictly stable.*

Proof. Multiplying the equations in (4.9) with ${\boldsymbol{v}^{(1)}}^* \tilde{H}$ and ${\boldsymbol{v}^{(2)}}^* \tilde{H}$, respectively, adding the transpose, and proceeding as in the analysis for the case of a free particle in 2-D, we end up with the following discrete energy estimate

$$
\begin{aligned}
\frac{d}{dt}\left(\|\boldsymbol{v}^{(1)}\|^2_{\tilde{H}} + \|\boldsymbol{v}^{(2)}\|^2_{\tilde{H}}\right) &= \boldsymbol{v}^{(1)^*}\tilde{H}\boldsymbol{v}_t^{(1)} + (\boldsymbol{v}_t^{(1)})^*\tilde{H}\boldsymbol{v}^{(1)} + \boldsymbol{v}^{(2)^*}\tilde{H}\boldsymbol{v}_t^{(2)} + (\boldsymbol{v}_t^{(2)})^*\tilde{H}\boldsymbol{v}^{(2)} \\
&= -\boldsymbol{v}^{(1)^*}\tilde{H}(AD_x + BD_y)\boldsymbol{v}^{(1)} + \boldsymbol{v}^{(1)^*}\tilde{H}(SAT^{(1)}) \\
&\quad - \boldsymbol{v}^{(1)^*}(AD_x + BD_y)^*\tilde{H}\boldsymbol{v}^{(1)} + (SAT^{(1)})^*\tilde{H}\boldsymbol{v}^{(1)} \\
&\quad - \boldsymbol{v}^{(2)^*}\tilde{H}(AD_x + BD_y)\boldsymbol{v}^{(2)} + \boldsymbol{v}^{(2)^*}\tilde{H}(SAT^{(2)}) \\
&\quad - \boldsymbol{v}^{(2)^*}(AD_x + BD_y)^*\tilde{H}\boldsymbol{v}^{(2)} + (SAT^{(2)})^*\tilde{H}\boldsymbol{v}^{(2)} \\
&\quad \underbrace{+\boldsymbol{v}^{(2)^*}\tilde{H}(\frac{i}{\hbar}V_0)\boldsymbol{v}^{(2)} + \boldsymbol{v}^{(2)^*}(\frac{i}{\hbar}V_0)^*\tilde{H}\boldsymbol{v}^{(2)}}_{=0} \\
&= BT_W + BT_I + BT_E + BT_S + BT_N
\end{aligned}
$$

where the boundary terms are as follows

Western boundary

$$
\begin{aligned}
BT_W = &\underbrace{\boldsymbol{v}_W^{(1)^*}(A_+ \otimes H)\boldsymbol{v}_W^{(1)} + \boldsymbol{v}_W^{(1)^*}(A_- \otimes H)\boldsymbol{v}_W^{(1)}}_{\text{from } SBP^{(1)}} \underbrace{-\boldsymbol{v}_W^{(1)^*}(A_+ \otimes H)(\boldsymbol{v}_W^{(1)} - \boldsymbol{g}_W)}_{\text{from } SAT_W^{(1)}} \\
&\underbrace{-(\boldsymbol{v}_W^{(1)^*} - \boldsymbol{g}_W)^*(A_+ \otimes H)\boldsymbol{v}_W^{(1)}}_{\text{from } (SAT_W^{(1)})^*} \\
= &\underbrace{\boldsymbol{v}_W^{(1)^*}(A_- \otimes H)\boldsymbol{v}_W^{(1)}}_{\leq 0} \underbrace{-(\boldsymbol{v}_W^{(1)} - \boldsymbol{g}_W)^*(A_+ \otimes H)(\boldsymbol{v}_W^{(1)} - \boldsymbol{g}_W)}_{\leq 0} + \underbrace{\boldsymbol{g}_W^*(A_+ \otimes H)\boldsymbol{g}_W}_{\text{known data}}
\end{aligned}
$$

Interface

$$
\begin{aligned}
BT_I = &\underbrace{-\boldsymbol{v}_I^{(1)^*}(A_+ \otimes H)\boldsymbol{v}_I^{(1)} - \boldsymbol{v}_I^{(1)^*}(A_- \otimes H)\boldsymbol{v}_I^{(1)}}_{\text{from } SBP^{(1)}} \\
&\underbrace{+\boldsymbol{v}_I^{(1)^*}(A_- \otimes H)(\boldsymbol{v}_I^{(1)} - \boldsymbol{v}_I^{(2)}) + (\boldsymbol{v}_I^{(1)} - \boldsymbol{v}_I^{(2)})^*(A_- \otimes H)\boldsymbol{v}_I^{(1)}}_{\text{from } SAT_I^{(1)}, (SAT_I^{(1)})^*} \\
&\underbrace{+\boldsymbol{v}_I^{(2)^*}(A_+ \otimes H)\boldsymbol{v}_I^{(2)} + \boldsymbol{v}_I^{(2)^*}(A_- \otimes H)\boldsymbol{v}_I^{(2)}}_{\text{from } SBP^{(2)}} \\
&\underbrace{-\boldsymbol{v}_I^{(2)^*}(A_+ \otimes H)(\boldsymbol{v}_I^{(2)} - \boldsymbol{v}_I^{(1)}) - (\boldsymbol{v}_I^{(2)} - \boldsymbol{v}_I^{(1)})^*(A_+ \otimes H)\boldsymbol{v}_I^{(2)}}_{\text{from } SAT_I^{(2)}, (SAT_I^{(2)})^*} \\
= &\underbrace{-(\boldsymbol{v}_I^{(1)} - \boldsymbol{v}_I^{(2)})^*(A_+ \otimes H)(\boldsymbol{v}_I^{(1)} - \boldsymbol{v}_I^{(2)})}_{\leq 0} + \underbrace{(\boldsymbol{v}_I^{(1)} - \boldsymbol{v}_I^{(2)})^*(A_- \otimes H)(\boldsymbol{v}_I^{(1)} - \boldsymbol{v}_I^{(2)})}_{\leq 0}
\end{aligned}
$$

Eastern boundary Similarly as for the western boundary and analogous to the one dimensional case, BT_E will be

$$
BT_E = \underbrace{-\boldsymbol{v}_E^{(2)^*}(A_+ \otimes H)\boldsymbol{v}_E^{(2)}}_{\leq 0} \underbrace{+(\boldsymbol{v}_E^{(2)} - \boldsymbol{g}_E)^*(A_- \otimes H)(\boldsymbol{v}_E^{(2)} - \boldsymbol{g}_E)}_{\leq 0} \underbrace{-\boldsymbol{g}_E^*(A_- \otimes H)\boldsymbol{g}_E}_{\text{known data}}
$$

Southern boundary

$$BT_S = \underbrace{\boldsymbol{v}_S^{(1)^*}(B_- \otimes H)\boldsymbol{v}_S^{(1)} + (\boldsymbol{v}_S^{(2)})^*(B_- \otimes H)\boldsymbol{v}_S^{(2)}}_{\leq 0}$$
$$\underbrace{-(\boldsymbol{v}_S^{(1)} - \boldsymbol{g}_S^{(1)})^*(B_+ \otimes H)(\boldsymbol{v}_S^{(1)} - \boldsymbol{g}_S^{(1)}) - (\boldsymbol{v}_S^{(2)} - \boldsymbol{g}_S^{(2)})^*(B_+ \otimes H)(\boldsymbol{v}_S^{(2)} - \boldsymbol{g}_S^{(2)})}_{\leq 0}$$
$$+ \underbrace{\boldsymbol{g}_S^{(1)^*}(B_+ \otimes H)\boldsymbol{g}_S^{(1)} + \boldsymbol{g}_S^{(2)^*}(B_+ \otimes H)\boldsymbol{g}_S^{(2)}}_{\text{known data}}$$

Northern boundary

$$BT_N = \underbrace{-\boldsymbol{v}_N^{(1)^*}(B_+ \otimes H)\boldsymbol{v}_N^{(1)} - \boldsymbol{v}_N^{(2)^*}(B_+ \otimes H)\boldsymbol{v}_N^{(2)}}_{\leq 0}$$
$$\underbrace{+(\boldsymbol{v}_N^{(1)} - \boldsymbol{g}_N^{(1)})^*(B_- \otimes H)(\boldsymbol{v}_N^{(1)} - \boldsymbol{g}_N^{(1)}) + (\boldsymbol{v}_N^{(2)} - \boldsymbol{g}_N^{(2)})^*(B_- \otimes H)(\boldsymbol{v}_N^{(2)} - \boldsymbol{g}_N^{(2)})}_{\leq 0}$$
$$- \underbrace{\boldsymbol{g}_N^{(1)^*}(B_- \otimes H)\boldsymbol{g}_N^{(1)} - \boldsymbol{g}_N^{(2)^*}(B_- \otimes H)\boldsymbol{g}_N^{(2)}}_{\text{known data}}$$

Thus, the discrete solution growth rate is bounded by the continuous growth rate and hence the semi-discretization (4.9) is strictly stable. □

4.4 Convergence study

To verify the performance of the discretization, an error convergence analysis is performed, using the same method and definitions as for the one dimensional case, in Section 3.4, except of course for the extra dimension and related implications. Again, the analytic plane wave solution derived in Section 2.1 is used as a reference solution, but we now consider an angle of incidence $\alpha = 30°$. The domain is composed by a rectangle with dimensions $x \in [0, 500]$nm, $y \in [0, 250]$nm. The error is analyzed at $t = 1 \cdot 10^{-13}$ s for each numerical solution, corresponding to the 257th time step, having each time step a size of $k = 3.8911 \cdot 10^{-16}s$, conservatively below the CFL condition. The results of the convergence study, which is otherwise carried out in the same way as for the one dimensional problem, are presented in Table 2. The achieved global convergence rate is $p + 1$ for an SBP operator of order $2p$, which was theoretically expected.

4.5 Simulations of Klein-tunneling

The transmission probability as a function of angle of incidence will look different for different fermion energies and for different barrier height energies. In our simulations we have used the energies presented in [3] - a fermion energy of 80 meV and a barrier height of 200 meV. An illustration of the simulated phenomenon for an angle of incidence of 15° is shown in Figure 5.

As in the one-dimensional case, it can be seen that the frequency of the wave-packet components changes within the barrier, increasing with the heighten of the barrier's potential. An additional observation in this two-dimensional case is that the direction of travel of the fermion changes within the barrier. This

Table 2: Error and error convergence rates, according to Eq. 3.13, for SBP operators with different orders of accuracy. Note that the global convergence rate is $p + 1$ for an SBP operator of order $2p$, which is expected, exactly as in the one dimensional case. The domain is 500 nm wide and 250 nm high.

N_x	N_y	2nd	$q^{(2)}$	4th	$q^{(4)}$	6th	$q^{(6)}$
41	21	9.19e-07		3.66e-07		2.36e-07	
81	41	3.18e-07	1.53	3.07e-08	3.57	3.21e-08	2.88
161	81	8.07e-08	1.98	2.68e-09	3.52	2.61e-09	3.62
321	161	2.02e-08	2.00	2.82e-10	3.25	1.74e-10	3.90
N_x	N_y	8th	$q^{(8)}$	10th	$q^{(10)}$		
41	21	2.66e-07		4.33e-07			
81	41	2.39e-08	3.48	3.56e-08	3.60		
161	81	8.78e-10	4.77	7.21e-10	5.63		
321	161	2.70e-11	5.02	1.21e-11	5.89		

suggests that a description similar to Snell's law for electromagnetic refraction could be appropriate also for describing Klein-tunneling in single-layer graphene, as discussed in [1].

This type of simulation was carried out with every integer angle of incidence between 0° and 75°. In this case 40 grid points per wave-length are used, which is sufficient to make the discretization errors negligible. The probability for the fermion to travel through the barrier is estimated for every angle by taking the transmitted mathematical energy and dividing it by the initial mathematical energy of the fermion. From this, the transmission probability as a function of angle of incidence can be computed. In Figure 6 the results are presented in a polar plot, which includes the theoretically expected transmission probability for the time-independent plane wave solution derived in [3]. As can be seen, the results do not agree, except for small angles of incidence, up to 15°.

This disagreement is probably due to the different approaches to the problem. Our approach takes into account the time-dependence and the fact that fermions have a finite size. In the simulations the Gaussian envelope used to create an initial wave-packet is about three wavelengths. Even though different widths were tested, the largest more than twice as big as the simulations in Figure 5, no significant change in transmission coefficient was observed. This suggests that the discrepancy is not caused by the localization but instead that it is due to the time-dependent approach to the problem.

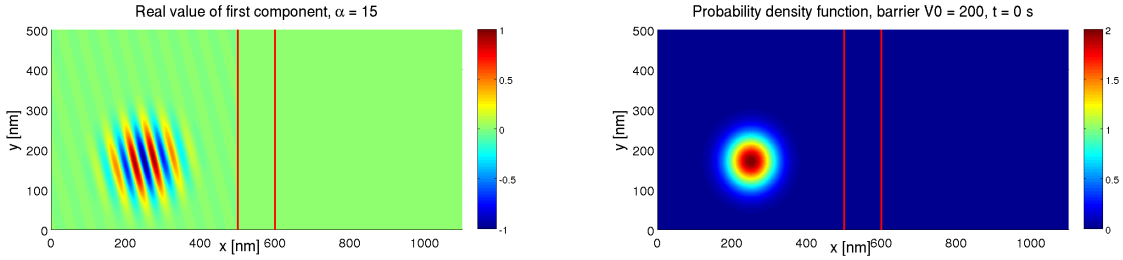

(a) Initial condition

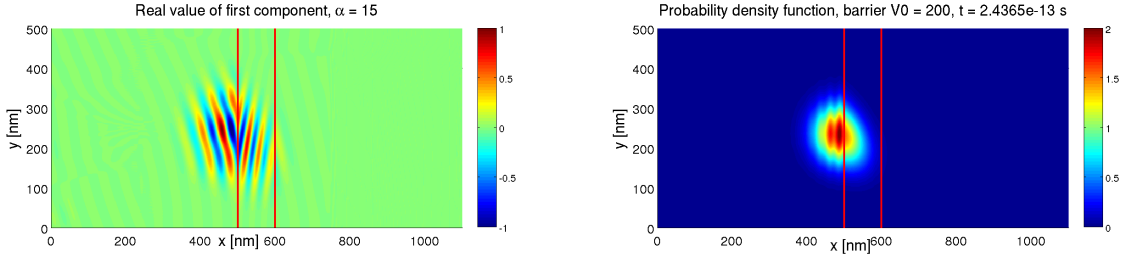

(b) $t = 2.4365 \cdot 10^{-13}$ s

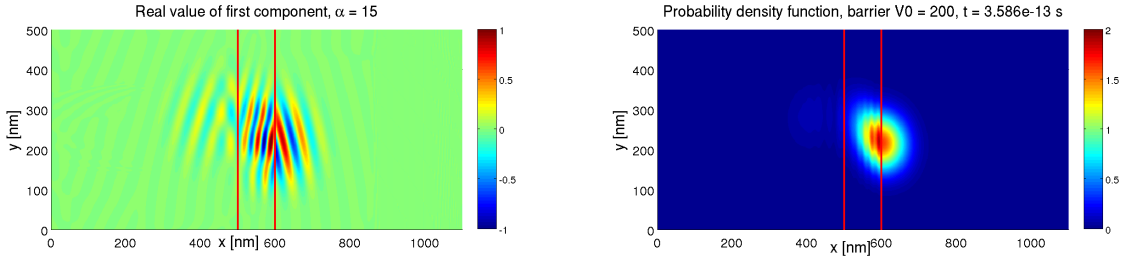

(c) $t = 3.586 \cdot 10^{-13}$ s

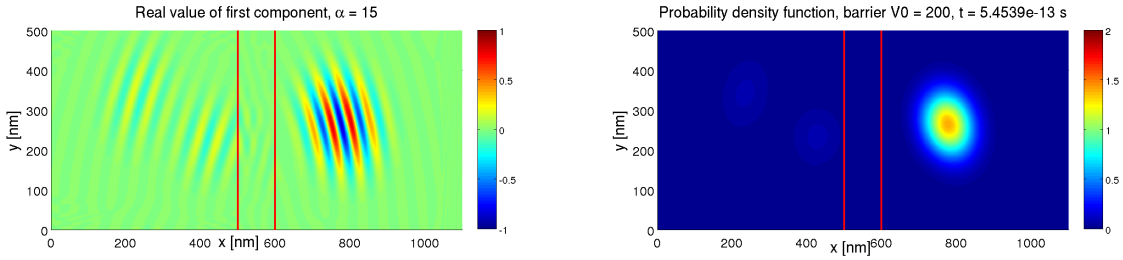

(d) $t = 5.4539 \cdot 10^{-13}$ s

Figure 5: To the right: a non-normalized probability density function of a simulated massless fermion of energy 80 meV, traveling in single-layer graphene towards a barrier of 200 meV, with an angle of incidence of 15°. To the left: the real part of the first component of the spinor. Note that there is a probability for the fermion to reflect back into the left domain when hitting the barrier.

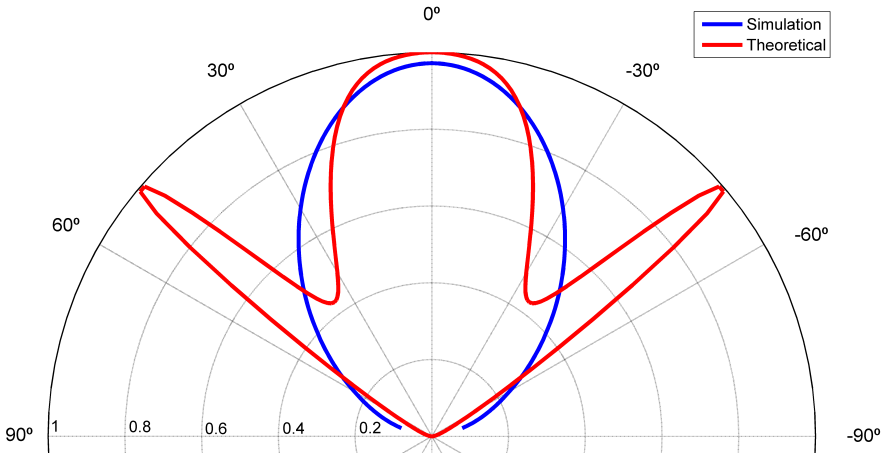

Figure 6: Transmission probability as function of the angle of incidence for a massless Dirac fermion of energy 80 meV and a barrier energy of 200 meV. Our numerical results for a tenth order semi-discretization in space and a fourth order Runge-Kutta as a time integrator (in blue) are compared with the analytic time-independent plane wave results from [3] (in red).

5 Conclusion

A strictly stable high-order accurate finite difference scheme for the simulation of time-dependent Klein-tunneling in single-layer graphene was constructed using the Summation-by-Parts–Simultaneous Approximation Term (SBP–SAT) method. The numerical simulations achieved a global error convergence rate of sixth order, using a tenth order SBP-operator, in agreement with the theoretical expectations.

The dynamics of Klein-tunneling in single-layer graphene were studied. We observed that the frequency of the components of the wave-packet changes within the barrier, depending on the height of the potential barrier. Moreover, in the two-dimensional case, the direction of travel of the fermion changes within the barrier, which suggests that a description similar to Snell's law for electromagnetic refraction could be appropriate also for describing Klein-tunneling in single-layer graphene, as discussed in [1].

We also compared the numerical transmission probabilities of time-dependent wave-packets across a potential barrier with the analytical plane wave time-independent results presented in [3], by computing the particle transmission probabilities for angles of incidence between 0^o and 75^o. The numerical time-dependent simulations do not agree with the theoretical stationary results. This discrepancy in the transmission probability may be due to the fact that, instead of plane waves, we model our particles more realistically as time-dependent moving wave-packets. Experiments with different wave-packet sizes indicate that localization is not responsible for the discrepancy, thus it must be caused by time-dependence. This suggests that time-dependent models are essential even for a qualitative understanding of Klein-tunneling in graphene.

6 Acknowledgments

The authors would like to thank their supervisor Martin Almquist for introducing them to the subject and for his constant support, Michael Thuné for sharing with them his experience in research on Scientific Computing and Maya Neytcheva for both her insightful comments and the nice mugs.

References

[1] P. E. Allain and J. N. Fuchs. Klein tunneling in graphene: optics with massless electrons. *The European Physical Journal B*, 83(3):301–317, October 2011.

[2] Martin Almquist, Ken Mattsson, and Tomas Edvinsson. High-fidelity numerical solution of the time-dependent Dirac equation. *Journal of Computational Physics*, 262:86–103, April 2014.

[3] M. I. Katsnelson, K. S. Novoselov, and a. K. Geim. Chiral tunnelling and the Klein paradox in graphene. *Nature Physics*, 2(9):620–625, August 2006.